THE INFLUENCE OF CLOUDINESS, TEMPERATURE AND PRECIPITATION VARIABILITIES ON SNOWMELT VARIATIONS IN THE WESTERN U.S.

Edwin Sumargo and Daniel R. Cayan

ABSTRACT

We investigate the influence of cloudiness variability on spring snowmelt and streamflow variations in the mountains of western U.S., and how it compares to that of precipitation (P), daily maximum and minimum temperature (T_{max} and T_{min}). We derive daily cloud albedo (α_{cloud}) from GOES visible albedo product to represent cloudiness. Daily snowmelt (ΔSWE) is obtained from 235 SNOTEL and CDEC snow water equivalent records. Daily streamflow fluctuations (ΔQ) are derived from 79 USGS/HCDN stream discharge records. Multivariate regression models are developed for five different sets: where α_{cloud}, P, T_{max} and T_{min} surface are predictors, and successively, where each one of the predictors is removed. α_{cloud}, T_{max}, T_{min} and P altogether account for 3%-62% of ΔSWE variance over Feb-Jul, averaging ~23%. The results further show the dominance of α_{cloud} influence, with increasing α_{cloud} role and decreasing T_{max}, T_{min} and P roles in warmer months and in drier years. Greater α_{cloud} contribution in dry years suggests the diminished importance of other hydrological factors in dry years, such as heavy precipitation events and fluctuations associated with higher snowpack. ΔQ responses to α_{cloud}, T_{max}, T_{min} and P exhibit similar patterns, but with lower explained variances. (KEYWORDS: cloudiness, snowmelt, streamflow, remote sensing, multivariate regression)

INTRODUCTION

The need of a robust understanding of snowmelt energy balance is a long-standing issue in snowmelt hydrology. One aspect underlying the need to resolve this issue is the fact that the link between solar radiation and hydrologic variability has not been thoroughly explored (Comola et al., 2015). The highly variable cloud cover—the primary regulator of the amount of solar radiation reaching the surface—is a major source of the difficulties in completing the energy balance. This problem has wide-ranging impacts on hydrologic applications, such as spring-to-summer water supply forecasting in the western United States (U.S.), where most of its water originates from the mountain snowmelt (Palmer, 1988; Serreze et al., 1999; Stewart et al., 2004). Moreover, complex mountain terrains and the snow-laden seasons hinder necessary installation, operation and maintenance of *in situ* solar radiation measurement network.

Various studies have demonstrated the applicability of satellite remote-sensing platforms to characterize hydroclimatic processes, such as cloud cover variability (Sumargo and Cayan, 2017), surface radiation (Lapo et al., 2017), snow cover area (Raleigh et al., 2011), etc. Our earlier work (Sumargo and Cayan, 2015) shows the applicability of Geostationary Operational Environmental Satellite (GOES) Albedo product, coupled with *in situ* snow and stream measurements, to characterize cloud cover variability and its influence on snowmelt and streamflow variability. However, cloudiness and other hydroclimatic variables may not be independent of each other. The purpose of this study is to offer a simple analysis to untangle the effect of cloudiness on snowmelt and streamflow variations from those of air temperature and precipitation, with an emphasis on snowmelt variations.

GEOGRAPHICAL STUDY AREA

Our study area is the western conterminous U.S. (WUS). WUS climate is characterized by warm and dry summer and cool and wet winter. The abundance of mountain terrains in WUS allows plenteous snowpack accumulation in the winter. Mountain streams flow from both rainfall and snowmelt. Precipitation runoff occurs immediately, while snowmelt runoff occurs more gradually, mostly during the warmer seasons (spring and summer) when the water is most needed for household uses, agricultures, etc. Consequently, the region's water supply relies substantially on spring-to-summer snowmelt-runoff (CADWR Bulletin 160-98; Cayan et al., 1998; Das et al., 2013).

In situ hydroclimatic measurement networks in the mountainous WUS have been available for decades, including the United States Geological Survey (USGS) stream discharge networks (http://waterdata.usgs.gov/nwis/)

Paper presented Western Snow Conference 2017
Scripps Institution of Oceanography, University of California San Diego, La Jolla, CA, 92037, esumargo@ucsd.edu

available since the early 20th century. Likewise, United States Department of Agriculture (USDA) Natural Resources Conservation Service Snow Telemetry (NRCS SNOTEL, http://www.wcc.nrcs.usda.gov/snow/) and California Department of Water Resources (CADWR) Cooperative Snow Survey (CSS) have maintained snow sensor networks for decades. In contrast, satellite observations are recent advancement and hence have been less widely used to study cloud cover variations and its influence on hydrologic variability (e.g., Simpson et al., 2004; Lapo et al., 2017).

Thus, WUS is suitable for our research objective. Following the domain of our satellite dataset (see DATA AND PROCESSING), we define WUS as the region spanning from 130°W to 113°W and 25°N to 50°N.

DATA AND PROCESSING

Cloud Albedo

We employ GOES (visible-band) albedo (α) product to derive cloud cover measure. The dataset spans from 1996-2015 and covers the westernmost conterminous U.S. (25°N - 50°N, 130°W - 113°W) with 4-km spatial resolution and 30-minute temporal resolution. The non-cloud component, i.e., clear-sky albedo (α_{clear}), is removed using clear-sky filtering operation to obtain cloud albedo (α_{cloud}):

$$\alpha_{cloud_{i,d,h}} = \alpha_{i,d,h} - \alpha_{clear_{i,d,h}} \quad [1]$$

where

$$\alpha_{clear_{i,d,h}} = \min(\alpha_{i,d-d_0,h} : \alpha_{i,d+d_0,h}) \quad [2]$$

following Paech et al. (2009), and subscripts *i*, *d*, and *h* represent GOES pixel, day, and hour of the day, respectively. Setting d_0 to 7 days is sufficient to capture α variations due to changing surface properties (Sumargo and Cayan, 2017). The daytime scenes (7-17 LST) are subsequently time-aggregated to produce daily α_{cloud}. The seasonal cycle of α_{cloud} is then removed (de-seasonalized) by subtracting its 29-day centered (±14 days) moving average of the daily climatology to focus on daily-to-intraseasonal processes. From here on, the de-seasonalized time-series are referred to as anomalies.

Precipitation, Maximum and Minimum Air Temperatures

We use Precipitation-elevation Regressions on Independent Slopes Model (PRISM) gridded precipitation (P), maximum and minimum air temperatures (T_{max} and T_{min}) (Daly, 2013). The dataset we use has 4-km spatial resolution and daily temporal resolution, and spans from 1996-2015. Similar to α_{cloud}, P, T_{max} and T_{min} are de-seasonalized using 29-day centered moving average of the daily climatology.

Snowmelt

We obtain 235 USDA/NRCS SNOTEL and CADWR/CSS (tabulated on California Data Exchange Center, http://cdec.water.ca.gov/) daily snow water equivalent (SWE) records to derive a proxy for snowmelt, defined as SWE difference between the day before and the day after (ΔSWE):

$$\Delta\text{SWE}_{i,d} = \text{SWE}_{i,d-1} - \text{SWE}_{i,d+1} \quad [3]$$

Subscripts *i* and *d* represent GOES pixel and day, respectively. Because we are interested in snowmelt events only, days with snow accumulation (ΔSWE < 0) are regarded as days with no snowmelt, so ΔSWE is set to zero for these days. From here on, ΔSWE refers to snowmelt. Similar to the other datasets, ΔSWE is de-seasonalized using 29-day centered moving average of the daily climatology. However, before de-seasonalization, ΔSWE is normalized by dividing the time-series by their water yearly amplitudes. Otherwise, high snowmelt events in dry years could register as negative anomalies, and vice versa. The GOES pixels and PRISM grids are interpolated to snow sensors coordinates using shortest distance method to find the pixels and grids corresponding to the snow sensors locations.

Streamflow

We utilize 79 USGS Hydroclimatic Data Network (HCDN) stream discharge (Q) records, compiled by Stewart et al. (2005) for snowmelt-dominated streams, to derive a proxy for streamflow, defined as Q difference between the day after and the day before (ΔQ):

$$\Delta Q_{i,d} = Q_{i,d-1} - Q_{i,d+1} \quad [4]$$

Subscripts i and d represent GOES pixel and day, respectively. ΔQ is then normalized in the same way as ΔSWE is. Similar to the other datasets, ΔQ is de-seasonalized using 29-day centered moving average of the daily climatology. The GOES pixels and PRISM grids are interpolated to stream gauges coordinates using shortest distance method to find the pixels and grids corresponding to the gauges locations.

METHODS

Multivariate Regression Models of Snowmelt and Streamflow

Figure 1 shows the lag-correlations between α_{cloud} and ΔSWE at Gin Flat, and between α_{cloud} and ΔQ at Merced River above Pohono Bridge, both situated in Idaho. The correlations illustrate that snowmelt's and streamflow's responses to cloudiness variations manifest gradually from day-0 to several days after the onset. Ultimately, this analysis reveals that, to quantify the influence of cloudiness variations on snowmelt and streamflow on a particular day, we also have to account for cloud cover fluctuations from several antecedent days. The same result is obtained for temperature and precipitations influences (not shown).

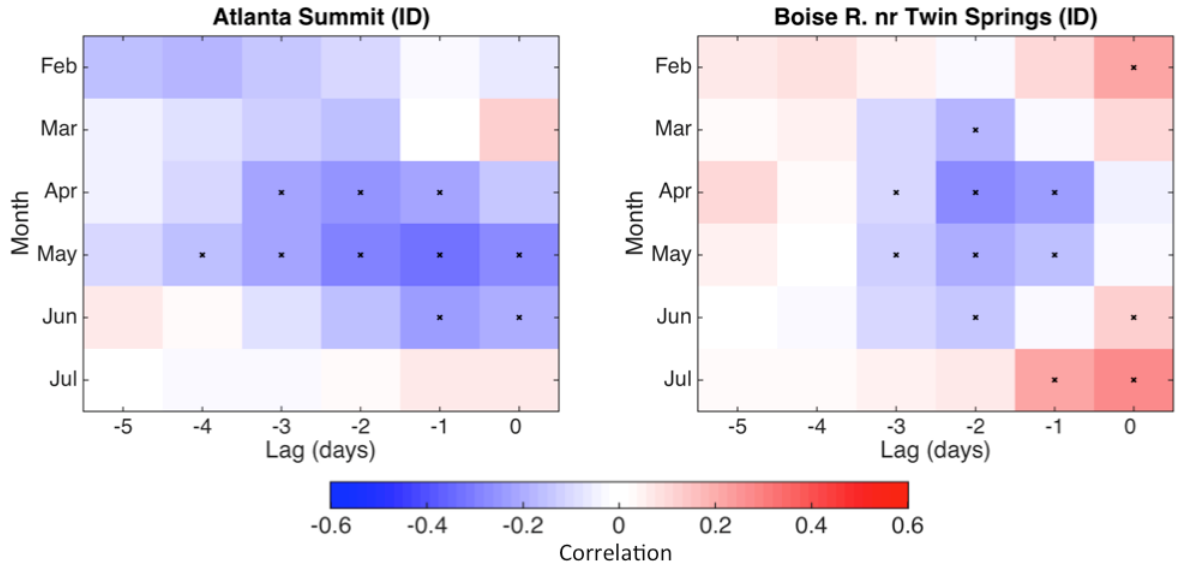

Figure 1. February-July lag-correlations (left) between α_{cloud} and ΔSWE at Atlanta Summit (43.76 °N, 115.24 °W, 2,310 m), and (right) between α_{cloud} and ΔQ at Boise River near Twin Springs (43.659 °N, 115.726 °W, 992 m), both located in Idaho. Lag < 0 means α_{cloud} leads ΔSWE, ΔQ. Positive correlation denotes snowmelt/streamflow increases with cloudiness, and vice versa. 'x' denotes where p-value < 0.01.

We construct multivariate linear regression models of ΔSWE and ΔQ with (z-scores of) overhead α_{cloud}, T_{max}, T_{min} and P as the predictors:

$$Y_{i,k,d} = \sum_j C_{i,j,d} * X_{i,j,d} + \varepsilon \quad [5]$$

where

$$X = z - scores\ of\ \text{overhead}\ \alpha_{cloud}, T_{max}, T_{min}, P$$
$$Y = \Delta\text{SWE}, \Delta Q$$
$$C = \text{regression coefficient}$$
$$\varepsilon = \text{error term}$$

We use the z-scores instead of the predictors themselves since the predictors have different means and variances. Subscripts *i, j, k* and *d* denote GOES pixel, predictor, model and day, respectively. To simplify the analysis, the predictors at day *d* are their time-averages from day $d–d_0$ to day *d*. Considering Figure 1, we set d_0 to 3 days as it sufficiently captures the lagged responses. For ΔSWE case, days where both SWE and ΔSWE are zero are excluded. The regression is then run and analyzed separately for each month from February to July, when snowmelt is most active. The predictive powers of the models are evaluated by computing the (adjusted) coefficients of determination (R^2) between modeled and observed ΔSWE and Δ*Q*. We will show R^2 as aggregates over WUS and four Western Snow Conference (WSC) divisions: North Pacific (NP), North Continental (NC), South Pacific (SP) and South Continental (SC) (https://westernsnowconference.org/about/committees).

To evaluate the contribution of each predictor, the regression analysis is run on five different model sets:

M1. Where α_{cloud}, T_{max}, T_{min} and *P* are the predictors,
M2. Where only T_{max}, T_{min} and *P* are the predictors,
M3. Where only α_{cloud}, T_{min} and *P* are the predictors,
M4. Where only α_{cloud}, T_{max} and *P* are the predictors, and
M5. Where only α_{cloud}, T_{max} and T_{min} are the predictors,

such that the difference in R^2 between:

M12. M1 and M2 estimates α_{cloud} contribution,
M13. M1 and M3 estimates T_{max} contribution,
M14. M1 and M4 estimates T_{min} contribution, and
M15. M1 and M5 estimates *P* contribution.

Dry/Wet Year Classification

The analysis above includes all years of 1996-2015. We subsequently partition the analysis into dry and wet years, identified using PRISM gridded *P* dataset. For each of the snow stations and stream gauges, the water year total *P* is computed, where 6 years with highest *P* are classified as wet years and 6 years with lowest *P* are classified as dry years.

RESULTS

Snowmelt Response to Cloud Cover, Precipitation, Maximum and Minimum Temperatures Variations

Figure 2 illustrates ΔSWE response to α_{cloud}, T_{max}, T_{min} and *P* variations in February, April and June. February map shows that the response is relatively small in early snowmelt season, with R^2 averaging ~16% evenly throughout WUS (Table 1). The small R^2 reflects the relatively low snowmelt activity in February, likely due to the combination of low temperature and solar insolation. The latter is especially important from cloud cover perspective, since the role of cloud shading upon snowpack is minimized during this period.

This number progressively increases with month. In March, the north-south asymmetry is evident with R^2 averaging ~18% in the north, and ~22% in the south, signifying earlier start of snowmelt activity in the south. By April, R^2 is roughly equivalent in NP, NC and SP, indicating active snowmelt events almost throughout WUS. The considerably lower R^2 in SC corresponds to the relatively dry condition and low SWE on our SC stations, which results in earlier peak SWE and snowmelt. In May, snowmelt activity declines in SP and SC, while it grows stronger in NP and NC, further indicating earlier peak snowmelt activity in the southwest.

By June, snowmelt activity is almost uniformly in decline throughout the region as denoted by the diminishing R^2, except in SC where R^2 grows to ~49%. The same growth is observed in NC and, to a lesser degree, in NP in July. A closer inspection shows that these high R^2 cases are accompanied by low numbers of stations involved in the analysis, as we only account for the locations with statistical significance at 99% level (*p*-value < 0.01). The few locations with *p*-value < 0.01 are the ones that typically have snowpack through early summer, suggesting that the analysis should be done with caution when snowpack is thin. In other words, at this point snowmelt is also limited by snow availability (Comola et al., 2015).

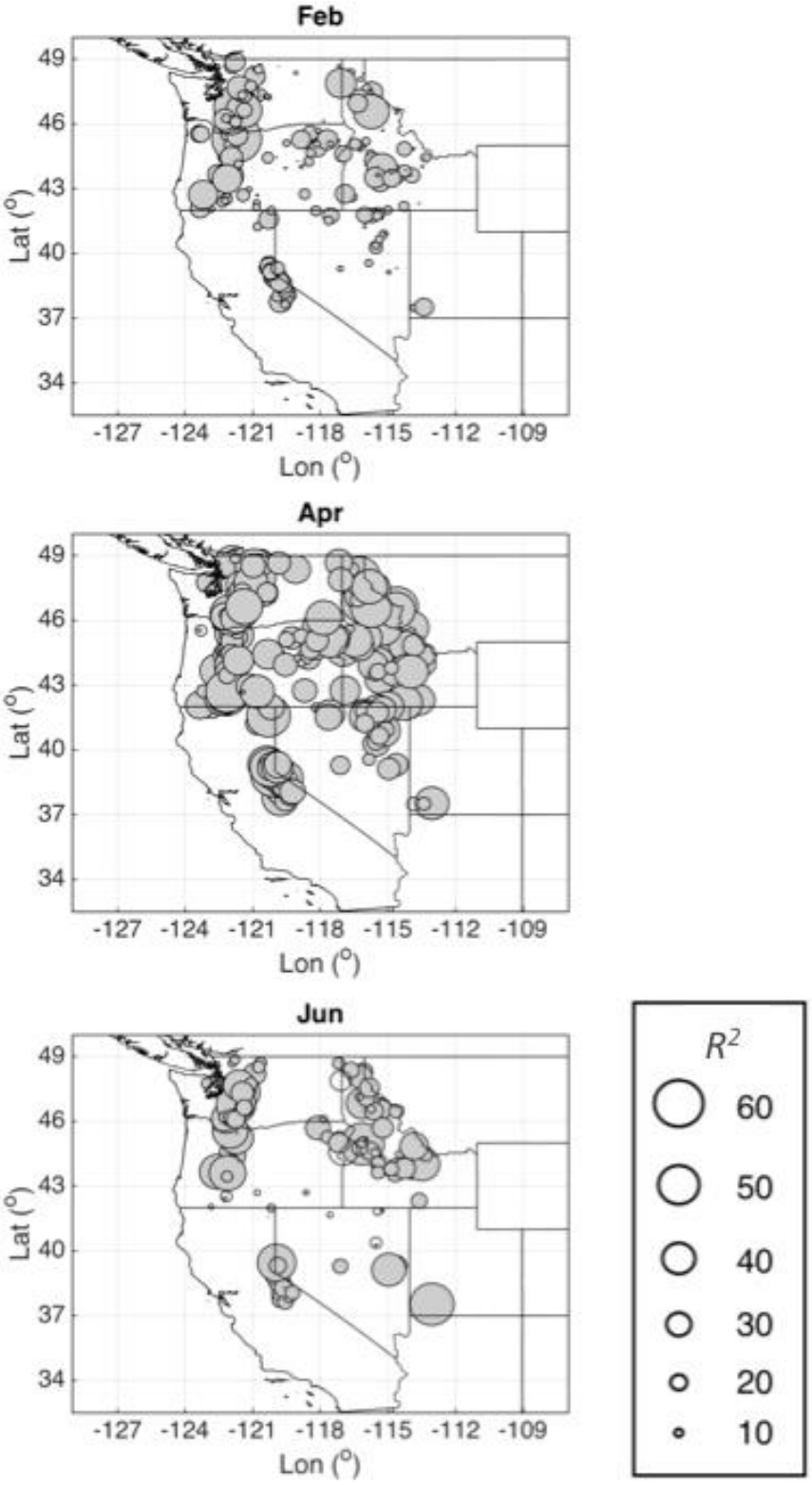

Figure 2. February, April and June R^2 maps showing the strength of model M1 in predicting ΔSWE. The strength of ΔSWE response to combined α_{cloud}, T_{max}, T_{min} and P variations is proportional to the size of the circle. Locations with p-value < 0.01 are shaded in gray.

Table 1. February-July R^2 showing the strength of ΔSWE response to α_{cloud}, T_{max}, T_{min} and P variations (model set M1), aggregated over WUS and WSC North Pacific (NP), North Continental (NC), South Pacific (SP) and South Continental (SC) regions. Only locations with p-value < 0.01 are accounted.

Month	Region				
	NP	NC	SP	SC	WUS
Feb	17	15	13	15	16
Mar	18	18	21	22	19
Apr	27	31	27	26	28
May	30	39	25	14	31
Jun	21	20	17	49	20
Jul	20	25	--	--	21

The Proportions of Cloud Cover, Precipitation, Maximum and Minimum Temperatures Contributions to Snowmelt Variation

The preceding analysis lumps α_{cloud}, T_{max}, T_{min} and P together. Here we apply four different scenarios described in the METHOD section to isolate the contribution of each predictor to ΔSWE variation. Table 2 displays similar R^2 statistics to that in Table 1, but for the four scenarios. M12 scenario shows similar trend to that in Table 1, where highest R^2 occurs in the mid-snowmelt season (~5%), and the high R^2 in June and July should be taken with caution as very few sites still have measureable snowpack. The relatively low R^2 in February-March (~2%) substantiates the minimal cloud-shading effect in early snowmelt season. Interestingly, the R^2 in NP and NC is higher in February than in March, although solar insolation and temperature are theoretically higher in March, which M13 and M14 scenarios support. In contrast, M15 scenario exhibits greatest R^2 in February (~3%), arguably because winter P events are relatively common in February. This result further suggests the higher R^2 in February in M12 scenario is related to P event or, in other words, rain-on-snow (ROS) event, which is frequent in the Pacific Northwest (McCabe et al., 2007).

M13 scenario surprisingly does not exhibit a strong trend in R^2. However, Table 2 shows that T_{max} is somewhat more important than α_{cloud} in February and March, reasonably since temperature fluctuation (longwave radiation) is relatively important for snowmelt in early snowmelt season when solar insolation is relatively low (Cristea et al., 2013). Likewise, M14 scenario does not show a clear seasonal signature. M15 scenario, on the other hand, displays higher R^2 in early snowmelt season, reflecting the more active winter P in early snowmelt season, which again, refers to ROS events.

Difference between Dry Years and Wet Years

The dry-wet year asymmetry is illustrated in Figure 3. In general, wet-year composite has greater R^2 in February and somewhat in March, while dry-year composite has greater R^2 in April onward. The larger R^2 in February in wet-year composite corresponds to the higher P in wetter years, as also shown by Table 2 that P is a relatively strong predictor during this month. On the other hand, the larger R^2 in the other months in dry-year composite is presumably related to the more frequent cloudy-clear sky transitions drier years, in contrast to the relatively persistent cloud cover in wetter years, which affect T_{max}, T_{min} and ultimately ΔSWE fluctuations.

Table 2. February-July R^2 differences between two ΔSWE model sets according to 4 different scenarios, aggregated over WUS and WSC North Pacific (NP), North Continental (NC), South Pacific (SP) and South Continental (SC) regions. Only locations with p-value < 0.01 are accounted.

Scenario	Month	Region				
		NP	NC	SP	SC	WUS
M12	Feb	2	2	1	-1	2
	Mar	0	1	1	5	1
	Apr	4	6	5	7	5
	May	4	6	2	2	4
	Jun	6	7	-1	--	5
	Jul	6	16	--	--	9
M13	Feb	2	2	2	1	2
	Mar	2	3	2	3	2
	Apr	3	2	2	6	2
	May	1	2	2	2	2
	Jun	2	0	2	-1	1
	Jul	4	-7	--	--	2
M14	Feb	1	1	2	1	1
	Mar	1	0	2	0	1
	Apr	2	2	1	6	2
	May	2	1	1	0	1
	Jun	2	1	1	2	2
	Jul	2	-7	--	--	0
M15	Feb	4	3	1	0	3
	Mar	1	1	0	1	1
	Apr	1	0	0	3	0
	May	0	0	1	0	0
	Jun	1	0	0	3	0
	Jul	0	0	--	--	0

Both dry-year and wet-year composites display peak R^2 in May. However, in dry-year composite, the high R^2 remains in June and vanishes in July, while in wet-year composite, R^2 progressively decreases after May and does not vanish in July. This pattern suggests a relatively well-defined peak snowmelt activity in dry years, and that snowmelt activity lasts longer in wet years, particularly in SP and SC as shown by both Figure 3 and Table 3.

When the four different scenarios are accounted, in February, M15 scenario exhibits the largest dry-wet year asymmetry, where R^2 tends to be larger in wet-year composite (Table 4), signifying the role of P in wet years. Towards mid-snowmelt season, the largest asymmetry is found in M12 scenario, where R^2 tends to be larger in dry-year composite, indicating the greater effect cloud shading (or the lack thereof) on snowmelt activity in dry years. A deeper investigation suggests that springtime α_{cloud} tends to be smaller in dry years, which can spur more rapid snowmelt by permitting more solar insolation reaching the surface. This result may also explain the relatively well-defined peak snowmelt activity in drier years. The same trend but with smaller magnitude difference between wet and dry years is found in M14 scenario (not shown). In contrast, M13 scenario exhibits higher mid-to-late spring R^2 in wet years, which highlights the relatively dominant T_{max} effect on snowmelt in wetter years when cloud cover is more persistent and solar insolation at the surface is lower.

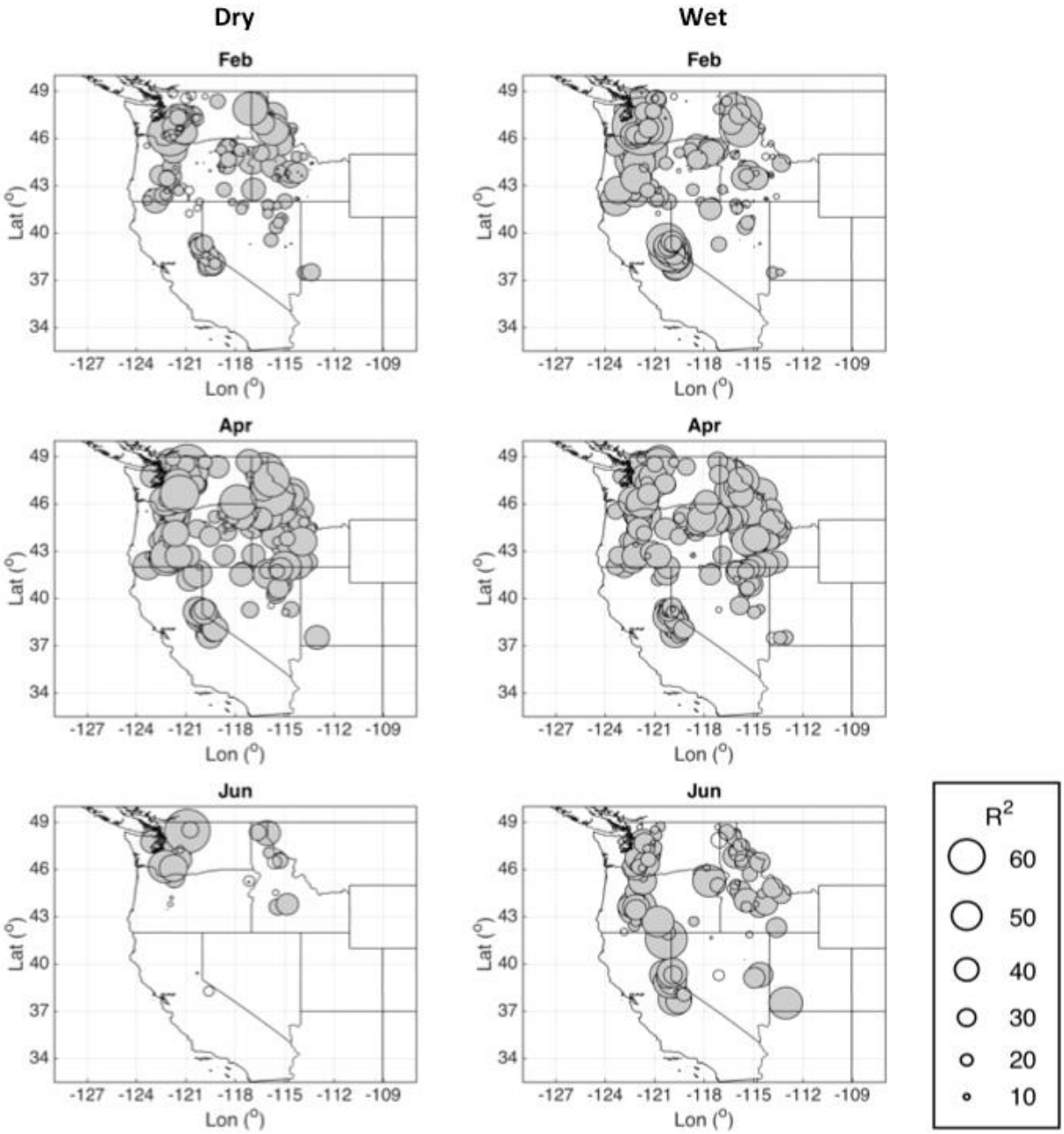

Figure 3. February, April and June R^2 maps showing the strength of model M1 in predicting ΔSWE, aggregated during dry years (left) and wet years (right). Locations with p-value < 0.01 are shaded in gray.

Table 3. February-July R^2 showing the strength of ΔSWE response to α_{cloud}, T_{max}, T_{min} and P variations (model set M1), time-aggregated over 6 driest and 6 wettest years, and spatially aggregated over WUS and WSC North Pacific (NP), North Continental (NC), South Pacific (SP) and South Continental (SC) regions. Only locations with p-value < 0.01 are accounted.

Water Year	Month	Region				
		NP	NC	SP	SC	WUS
Dry	Feb	28	28	21	24	25
	Mar	26	25	25	31	25
	Apr	32	34	30	37	32
	May	37	40	28	--	36
	Jun	36	26	--	--	33
	Jul	--	--	--	--	--
Wet	Feb	35	32	31	15	33
	Mar	27	23	27	19	26
	Apr	31	34	26	21	30
	May	34	44	25	16	35
	Jun	26	25	31	51	27
	Jul	27	28	--	--	27

Streamflow Response

ΔQ response to α_{cloud}, T_{max}, T_{min} and P variations are significantly smaller that the ΔSWE counterpart (Figure not shown), plausibly because streamflow is a convolution of many more variables, such as evaporation, local and upstream snowmelt-runoff, groundwater exfiltration and interflow, soil moisture, etc. (Bras, 1990; Woodhouse, 2016). Nevertheless, Table 5 shows that despite the small R^2 fluctuation throughout the snowmelt season, R^2 has a peak in May, consistent with ΔSWE case. Table 5 also indicates that R^2 is higher in February than in March.

When applied to ΔQ case, the same four scenarios as in Table 2 show similar patterns (Table not shown), which suggest the role of P in February. Different from ΔSWE, however, M13 and M14 display somewhat more defined seasonal structure, with highest R^2 in April and May, respectively. Furthermore, while ΔSWE case shows a problem when SWE is low or non-existent in June-July, ΔQ case does not seem to show the same problem when the Q is low during this period. While R^2 is relatively low during this period, inasmuch as snowmelt-runoff has diminished, ΔQ fluctuation remains largely active owing to the base flow, evaporation, summer convective P, groundwater-related activities, etc.

The dry/wet years' asymmetry in ΔQ case exhibits identical patterns to that in ΔSWE case, including lower magnitudes of R^2 and its fluctuation, are observed. Consistent with ΔSWE case, the outcome demonstrates earlier spring onset and earlier drying effect of summertime in drier years.

Table 4. February-July R^2 differences between two ΔSWE model sets according to scenarios M12 and M15, time-aggregated over 6 driest and 6 wettest years, and spatially aggregated over WUS and WSC North Pacific (NP), North Continental (NC), South Pacific (SP) and South Continental (SC) regions. Only locations with p-value < 0.01 are accounted.

Scenario	Water Year	Month	Region				
			NP	NC	SP	SC	WUS
M12	Dry	Feb	13	14	8	8	11
		Mar	7	8	5	15	7
		Apr	9	8	8	18	9
		May	11	7	6	--	10
		Jun	21	13	--	--	18
		Jul	--	--	--	--	--
	Wet	Feb	20	18	18	0	19
		Mar	9	6	7	3	8
		Apr	7	8	4	2	7
		May	9	11	3	3	8
		Jun	11	12	13	--	12
		Jul	13	19	--	--	15
M15	Dry	Feb	4	3	1	0	2
		Mar	3	2	1	2	2
		Apr	1	1	1	0	1
		May	1	0	1	--	1
		Jun	1	3	--	--	2
		Jul	--	--	--	--	--
	Wet	Feb	8	6	5	0	7
		Mar	4	2	0	-2	2
		Apr	3	2	1	0	2
		May	1	0	1	1	1
		Jun	2	-1	1	6	1
		Jul	0	0	--	--	0

Table 5. Same as Table 1, except for ΔQ.

Month	Region				
	NP	NC	SP	SC	WUS
Feb	7	4	8	8	7
Mar	7	6	7	7	7
Apr	13	10	8	14	11
May	10	9	9	12	10
Jun	7	5	7	8	7
Jul	7	7	6	10	7

CONCLUSIONS

The influence of cloud cover, temperature and precipitation variability on snowmelt variation is significant, particularly in May when the variability accounts for ~31% of snowmelt variation. When the effect of individual predictor is partitioned, precipitation dominates the influence in February when both solar insolation and temperatures are low, indicating the role of rain-on-snow event on snowmelt. Thereafter, cloudiness dominates the influence in mid-to-late spring when solar radiation is increasingly important to snowmelt energy balance. The role of temperature is moderate, which is somewhat surprising since daytime temperature is significant in snowmelt energy balance during colder months when solar insolation is low (Cristea et al., 2013), especially in forested environment (Lundquist et al., 2013), and since nighttime temperature is instrumental for snowpack refreezing (Bengtsson, 1982).

When wet/dry-year factor is accounted, in early spring, the cumulative influence of the predictors is stronger in the wet-year composite. As expected, precipitation is dominant in the wet-year composite, which may explain the relatively strong influence during this period. The trend is reversed in mid-to-late spring when it is stronger in the dry-year composite, possibly because of the more frequent clear/cloudy sky interludes in drier years. Accordingly, we find that cloudiness influence is stronger in the dry-year than in the wet-year composite, while daytime temperature effect is stronger in the wet-year than in the dry-year composite during this period. In both composites, cloudiness is the dominant predictor. Furthermore, snowmelt response has a well-defined seasonal structure in drier years, with strong response in mid-spring and an abruptly diminishing response toward early summer. In contrast, the seasonal structure of snowmelt response is less pronounced, but lasts longer through early summer, possibly reflecting the more abundant snow in wetter years. These structures reveal the different snowmelt dynamics from dry years to wet years, signifying the impact of inter-annual hydroclimate variability on snowpack.

Lastly, we show that streamflow response to cloud cover, temperature and precipitation variations is identical to snowmelt response. However, the lower response magnitude compared to that of snowmelt indicates the more complex nature of streamflow processes involving more variables, such as groundwater and upstream processes.

ACKNOWLEDGEMENTS

We thank California Department of Water Resources (Contract #4600010378, AM-04) for providing support for ES. We also thank California Energy Commission, and Southwest Climate Science Center for providing support for DRC.

REFERENCES

Bengtsson, L. 1982. The importance of refreezing on the diurnal snowmelt cycle with application to a northern Swedish catchment, *Hydrology Research*, *13*(1), 1-12.

Bras, R. L. 1990. *Hydrology: an introduction to hydrologic science*, Addison-Wesley, Reading, Mass.

California Department of Water Resources. 1998. Bulletin 160-98, http://www.waterplan.water.ca.gov/previous/b160-98/TOC.cfm.

Cayan, D. R., M. D. Dettinger, H. F. Diaz, and N. E. Graham. 1998. Decadal variability of precipitation over western North America. *Journal of Climate*, *11*, 3148-3166.

Comola, F., B. Schaefli, P. Da Ronco, G. Botter, M. Bavay, A. Rinaldo, and M. Lehning. 2015. Scale-dependent effects of solar radiation patterns on the snow-dominated hydrologic response, *Geophysical Research Letter*, *42*, doi:10.1002/2015GL064075.

Cristea, N. C., J. D. Lundquist, S. P. Loheide, C. S. Lowry, and C. E. Moore. 2013. Modelling how vegetation cover affects climate change impacts on streamflow timing and magnitude in the snowmelt-dominated upper Tuolumne Basin, Sierra Nevada, *Hydrological Processes*, doi:10.1002/hyp.9909.

Lapo, K. E., L. M. Hinkelman, E. Sumargo, M. Hughes, and J. D. Lundquist. 2017. A critical evaluation of modeled solar irradiance over California for hydrologic and land surface modeling, *Journal of Geophysical Research: Atmosphere*, *122*, 299-317, doi:10.1002/2016JD025527.

Lundquist, J. D., S. E. Dickerson-Lange, J. A. Lutz, J. A., and N. C. Cristea. 2013. Lower forest density enhances snow retention in regions with warmer winters: A global framework developed from plot-scale observations and modeling, *Water Resources Research*, *49*(10), 6356-6370.

McCabe, G. J., L. E. Hay, and M. P. Clark. 2007. ROS Events in the Western United States, *Bulletin of American Meteorological Society*, *88*, 319–328. doi: http://dx.doi.org/10.1175/BAMS-88-3-319.

Paech, S. J., J. R. Mecikalski, D. M. Sumner, C. S. Pathak, Q. Wu, S. Islam, and T. Sangoyomi. 2009. A calibrated, high-resolution GOES satellite solar insolation product for a climatology of Florida evapotranspiration, *Journal of the American Water Resources Association*, *45*(6), 1328–1342.

Palmer, P. L. 1988. The SCS snow survey water supply forecasting program: Current operations and future directions, *Proc. Western Snow Conf.*, pp. 43–51.

Raleigh, M. S., K. Rittger, and J. D. Lundquist. 2011. What lies beneath? Comparing MODIS fractional snow covered area against ground-based observations under forest canopies and in the meadows of the Sierra Nevada. *Proc. Western Snow Conf.*, *79*, pp. 3-14.

Serreze, M. C., M. P. Clark, R. L. Armstrong, D. A. McGinnis, and R. S Pulwarty. 1999. Characteristics of the western United States snowpack from snowpack telemetry (SNOTEL) data, *Water Resources Research*, *35*(7), 2145-2160.

Stewart, I. T., D. R. Cayan, and M. D. Dettinger. 2005. Changes towards earlier streamflow timing across western North America, *Journal of Climate*, *18*, 1136-1155.

Sumargo, E., and D. R. Cayan. 2015. Variability of cloud cover and its relation to springtime snowmelt and runoff, *Proceeding of the Western Snow Conf*erence, *83*, pp. 77-87. [Available at https://westernsnowconference.org/files/PDFs/2015Sumargo.pdf]

Sumargo, E., and D. R. Cayan. 2017. Variability of Cloudiness over Mountain Terrain in the Western United States, *Journal of Hydrometeorology*, doi:10.1175/JHM-D-16- 0194.1, *in press.*

Stewart, I., D. R. Cayan, and M. D. Dettinger. 2004. Changes in snowmelt runoff timing in western North America under a 'Business as Usual' climate change scenario, *Climatic Change*, ***62***(1), 217-232.

Woodhouse, C. A., G. T. Pederson, K. Morino, S. A. McAfee, and G. J. McCabe. 2016. Increasing influence of air temperature on upper Colorado River streamflow, *Geophysical Reserach Letter, 43*, 2174–2181, doi:10.1002/2015GL067613.